Science Arts & Métiers (SAM)
is an open access repository that collects the work of Arts et Métiers Institute of Technology researchers and makes it freely available over the web where possible.

This is an author-deposited version published in: https://sam.ensam.eu
Handle ID: .http://hdl.handle.net/10985/25041

To cite this version :

Xiaoxiao DU, Qiang CHEN, George CHATZIGEORGIOU, Fodil MERAGHNI, Wei WANG, Gang ZHAO - Isogeometric homogenization of unidirectional nanocomposites with energetic surfaces - Acta Mechanica p.19p. - 2024

Any correspondence concerning this service should be sent to the repository
Administrator : scienceouverte@ensam.eu

Xiaoxiao Du · **Qiang Chen** · **Chatzigeorgiou George** ·
Fodil Meraghni · **Wei Wang** · **Gang Zhao**

Isogeometric homogenization of unidirectional nanocomposites with energetic surfaces

Abstract The present work aims to propose an interface-enriched isogeometric analysis strategy for predicting the size-dependent effective moduli and local stress field of periodic arrays of nanosize inhomogeneity. The proposed framework allows for an exact representation of the curved boundary of inhomogeneity inside the matrix due to the representation of the geometry of repeating unit cells for microstructured materials with nonuniform rational B-splines. The energetic surface was characterized by the Gurtin–Murdoch model, and it was incorporated into the proposed framework by introducing additional surface energies linked to the bulk elements neighbouring the interface. The surface-enhanced isogeometric homogenization method was verified through comparisons with existing solutions found in the literature. It is demonstrated that the proposed framework enables the satisfaction of higher-order continuity of the displacement fields, leading to smooth and accurate predictions of the stress fields and homogenized moduli of nanocomposites, without encountering the convergence problems associated with conventional finite-element methods in the literature.

1 Introduction

The interface between different phases is actively engaged in determining the local stress concentration within the microstructures, thus the global elastic/inelastic behaviour of composites to thermomechanical loading. From a mechanics point of view, the interface can be perceived as a surface with negligible thickness, allowing it to be treated as a two-dimensional manifold in equilibrium. One common approach to model interface behaviour is to consider perfect bonding between various phases. The perfect interface model posits that no discontinuity in either displacement or traction is permitted along the interface that separates distinct phases. Most often, the physical nature of the interfacial region cannot be adequately captured by the perfect interface model due to the presence of defects arising from the manufacturing process or the occurrence of damage in the affected region upon external loading, among others.

Therefore, imperfect interface models have been frequently employed to better represent the actual adhesion state of the inclusion and matrix phases, accounting for the kinematic or kinetic relations of interface regions [1–6]. In the energetic interface or the so-called coherent interface, the discontinuity in terms of tractions is

X. Du · W. Wang · G. Zhao
School of Mechanical Engineering and Automation, Beihang University, Beijing 100191, People's Republic of China

Q. Chen (🖂)
School of Mechanical Engineering, Xi'an Jiaotong University, Xi'an 710049, Shaanxi, People's Republic of China
e-mail: qiangchen@xjtu.edu.cn; kirkcq@gmail.com

Q. Chen · C. George · F. Meraghni
Arts et Métiers Institute of Technology, CNRS, Université de Lorraine, LEM3-UMR7239, F-57000 Metz, France

G. Zhao
Tsinghua University, Beijing 100084, People's Republic of China

allowed, while the continuity in terms of displacements is preserved. To describe the stress transfer mechanisms of energetic interfaces in continuum mechanics, the Gurtin and Murdoch [7, 8] interface theory was adopted in the literature. In this model, the equilibrium of the interfacial stresses is governed by the traction jump conditions expressed in terms of the Young–Laplace equations [9]. An alternative to the elastic interface is the cohesive interface model [10, 11]. The latter takes into account displacement discontinuity while maintaining the traction continuity condition despite physical separation. It suffices to express the interfacial tractions into normal and tangential components and assume they are functions of normal and tangential displacement discontinuities at the interface [12]. In a more general case, the general interface model is allowed to develop both traction and displacement continuities [1, 13, 14]. Evidently, the general interface model simplifies to either the elastic interface model or the cohesive interface model in the limit. It is an ideal framework to model the surface effect and failure of the interface in an integrated manner. For the recent developments and applications of imperfect interface models for heterogeneous solids, we refer to the review articles by [2, 15, 16].

This manuscript focuses on the study of the impact of energetic surfaces on the homogenized mechanical properties of periodic nanostructured materials and the local stress field distributions to mechanical loading. At the nanoscale, the presence of interfacial stresses and energies in nanocomposites is well recognized, which arises due to variations in configuration and coordination numbers between surface atoms and those in the neighbouring bulk materials [17, 18]. The interfacial stresses render the effective elastic/inelastic stress–strain response and local deformation of periodic arrays of fibers/porosities size-dependent at the scale of nanometres. To quantify the interface effect on the size-dependent response of nanoscale component architectures, a number of researchers have employed molecular dynamic simulations. While these MD simulations have been demonstrated to be useful tools for verifying the applicability and accuracy of the elastic interface model which accounts for nanoscale surface effects and surface parameter calibration for surface-enhanced continuum-level computational models [19], they are inefficient and unsuitable for analysing nanoscale architectured materials across a wide range of parameters and dimensions due to significant computational expenses.

To address the issue with the MD methods, classical mean-field micromechanics approaches enriched with the Gurtin–Murdoch interface have been adopted by many investigators to enhance comprehension of the surface's impact on the homogenized moduli of nanocomposites, such as the Mori–Tanaka (MT), composite cylinder/sphere assemblage models (CCA) and three phase models [17, 20–22]. These models are based on simplified geometric representations of composites with cylindrical fibers or spherical inclusions in the matrix. The explicit expressions can be derived in terms of homogenized moduli with surface parameters and fiber radius. However, the simple solutions fail to account for the adjacent fiber/pore interactions. They substantially underestimate the local stress distributions within the matrix phase, yielding inaccurate homogenized moduli at high-volume content.

To accurately predict the impact of energetic surfaces on the mechanical response of nanocomposites, new full-field homogenization approaches demanding more advanced analytical or numerical techniques continue to emerge. For instance, Wang et al. [23] introduced the locally exact homogenization technique grounded in elasticity theory for square and hexagonal unit cells containing cylindrical fiber/porosity. The accuracy of the technique relied on periodic boundary displacement and traction constraints established through a new balanced variational principle. The interface behaviour was described by the Gurtin–Murdoch interface model, and the interfacial traction continuity condition between the fiber/matrix was replaced by the Young–Laplace condition. Chen et al. [24, 25] proposed a finite-volume micromechanics approach for predicting homogenized moduli, elastoplastic stress–strain response, and local stress fields of periodic arrays of cylindrical porosity. In this approach, finite-difference approximations were used to calculate the partial derivatives found in the Young–Laplace equations for interfacial stress equilibrium at the interfaces between the energetic surface and the discretized matrix. The Gurtin–Murdoch interface model has also been successfully incorporated into the finite-element framework by many authors [26–29]. For this, the Gurtin–Murdoch interface model was incorporated by considering supplementary surface energies linked to the elements along the boundaries of the pores. The above solution methods enable the incorporation of adjacent inclusion interactions through periodic boundary conditions. An alternative approach for accounting for such interaction is the elasticity-based homogenization scheme, called the equivalent inhomogeneity technique (EIT), proposed by Mogilesvkaya et al. [30, 31]. The EIT technique entails solving for the displacement and stress fields in both the matrix and the cluster of fibers, subject to homogeneous boundary conditions.

In this manuscript, an interface-enhanced isogeometric analysis framework [32, 33] has been developed to enhance the homogenization and localization of periodic arrays of nanoporosities with energetic surfaces. The proposed framework enables the satisfaction of higher-order continuity of the displacement fields, yielding accurate and smooth stress field predictions akin to the theory of elasticity. Hence, the proposed framework is particularly well-suited for modelling the surface effect in composites where significant deformation and stress gradients are encountered. In addition, the isogeometric homogenization technique employs the nonuniform rational B-splines (NURBS) for representing the geometry of repeating unit cells for multiphased materials, allowing for an exact representation of the curved boundary of the fiber/porosity inside the matrix. The main novelties of the present work include:

- Construction of an isogeometric homogenization technique for nanoporous composites by incorporating the surface elasticity model modelled via the Gurtin–Murdoch interface theory
- Extensive validation of the IGH-generated homogenized moduli and local stress fields against the various benchmark solutions
- Demonstration that the IGH technique facilitates smoother and more accurate field approximations over the conventional FEM methods, without sacrificing the computational efficiency

2 Coherent interface overview

In this section, the coherent interface model employed for modelling the size-dependent effect in nanocomposites is recalled. This lays a foundation for the development of the isogeometric analysis-based homogenization approach incorporating surface elasticity, which is presented in the next section.

Figure 1 illustrates a unidirectional composite containing nanosized cylindrical fibers of the same radius that are dispersed in the matrix media. The constitutive equation for a linearly elastic solid under infinitesimal deformations and rotations can be written as:

$$\boldsymbol{\sigma}^{(q)} = \mathbf{C}^{(q)} \cdot \boldsymbol{\varepsilon}^{(q)} \tag{1}$$

where

$$\boldsymbol{\varepsilon}^{(q)} = \frac{1}{2}\left(\nabla\mathbf{u}^{(q)} + \nabla\mathbf{u}^{\mathrm{T}(q)}\right) \tag{2}$$

where $\boldsymbol{\sigma}^{(q)} = [\sigma_{11}, \sigma_{22}, \sigma_{33}, \sigma_{23}, \sigma_{13}, \sigma_{12}]^{(q)\mathrm{T}}$ denote stresses, $\boldsymbol{\varepsilon}^{(q)} = [\varepsilon_{11}, \varepsilon_{22}, \varepsilon_{33}, 2\varepsilon_{23}, 2\varepsilon_{13}, 2\varepsilon_{12}]^{(q)\mathrm{T}}$ denote strains, and $\mathbf{u}^{(q)} = [u_1, u_2, u_3]^{(q)\mathrm{T}}$ denotes displacements. ∇ indicates the gradient operator. $\mathbf{C}^{(q)}$ represents the fourth-order elastic stiffness tensor. The superscripts $q = 0, 1$ indicate, respectively, the matrix and inhomogeneities. The elastic stiffness tensor for transversely isotropic constituent phases can be represented by Hill's elastic moduli [34], if the axis of symmetry is paralleled to the global x_1 axis:

$$\mathbf{C}^{(q)} = \begin{bmatrix} n & l & l & 0 & 0 & 0 \\ l & k+m & k-m & 0 & 0 & 0 \\ l & k-m & k+m & 0 & 0 & 0 \\ 0 & 0 & 0 & m & 0 & 0 \\ 0 & 0 & 0 & 0 & p & 0 \\ 0 & 0 & 0 & 0 & 0 & p \end{bmatrix}^{(q)} \tag{3}$$

where n, l, k, m and p indicate unit uniaxial straining constant, cross-constant, the plane strain bulk constant, transverse shear constant, and axial shear constant, respectively.

It is assumed the presence of a zero-thickness energetic interface that separates the inhomogeneities and the surrounding matrix materials. Within this interface, a distinct constitutive equation governs its behaviour with the plane stress assumption, reflecting the unique energy state of its atoms or molecules compared to the bulk material to which it is closely attached., cf., Gurtin and Murdoch [7, 8]. In this document, we only consider a cylindrical inhomogeneity with a constant radius a. It is assumed that the interface's normal direction is parallel to the local axis r in cylindrical coordinates (z, r, θ). The constitutive relation of the interface can be described by:

$$\tilde{\boldsymbol{\sigma}}^{(2)} = \tilde{\mathbf{C}}^{(2)} \cdot \tilde{\boldsymbol{\varepsilon}}^{(2)} \tag{4}$$

where the subscript (2) indicates the energetic surface, and

$$\tilde{\boldsymbol{\sigma}}^{(2)} = \begin{bmatrix} \sigma_{zz} \\ \sigma_{\theta\theta} \\ \sigma_{\theta z} \end{bmatrix}^{(2)}, \tilde{\boldsymbol{\varepsilon}}^{(2)} = \begin{bmatrix} \varepsilon_{zz} \\ \varepsilon_{\theta\theta} \\ 2\varepsilon_{\theta z} \end{bmatrix}^{(2)}, \tilde{\mathbf{C}}^{(2)} = \begin{bmatrix} C_{11} & C_{13} & 0 \\ C_{13} & C_{33} & 0 \\ 0 & 0 & C_{55} \end{bmatrix}^{(2)} \tag{5}$$

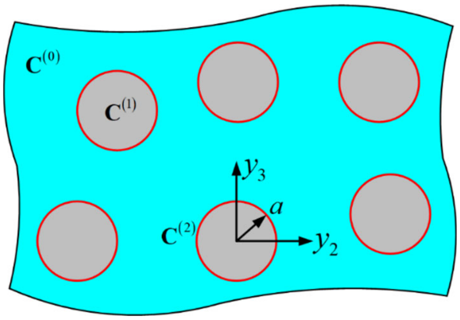

Fig. 1 Illustration of unidirectional composites with the energetic interface (highlighted in red) inside the matrix phase

where $C_{11}^{(2)} = C_{33}^{(2)} = \lambda^{(2)} + 2\mu^{(2)}$, $C_{13}^{(2)} = \lambda^{(2)}$ and $C_{13}^{(2)} = \mu^{(2)}$ are the surface moduli. The tilde symbol indicates cylindrical coordinate quantities.

The second critical assumption within the Gurtin–Murdoch interface model asserts that the interface is kinematically coherent, signifying that there are no atomic bonds disrupted along the surface that separates the inhomogeneities and matrix phases. Specifically, the continuity of the interface necessitates that the tangential and axial strain components remain consistent across it.:

$$\begin{bmatrix} \varepsilon_{zz} \\ \varepsilon_{\theta\theta} \\ \varepsilon_{\theta z} \end{bmatrix}^{(2)} = \begin{bmatrix} \varepsilon_{zz} \\ \varepsilon_{\theta\theta} \\ \varepsilon_{\theta z} \end{bmatrix}^{(1)} = \begin{bmatrix} \varepsilon_{zz} \\ \varepsilon_{\theta\theta} \\ \varepsilon_{\theta z} \end{bmatrix}^{(0)} \tag{6}$$

The stress tensors $\boldsymbol{\sigma}^{(q)} (q = 0,\ 1)$ in the fiber and matrix obey the following equilibrium equations:

$$\nabla \cdot \boldsymbol{\sigma}^{(q)} = \mathbf{0} \tag{7}$$

where $\nabla\cdot$ denotes the divergence operation. The interfacial stresses in equilibrium require that:

$$\begin{aligned} &-\frac{\sigma_{\theta\theta}^{(2)}}{a} + [\![\sigma_{rr}]\!] = 0 \\ &\frac{1}{a}\frac{\partial \sigma_{\theta\theta}^{(2)}}{\partial \theta} + \frac{\partial \sigma_{\theta z}^{(2)}}{\partial z} + [\![\sigma_{r\theta}]\!] = 0 \\ &\frac{1}{a}\frac{\partial \sigma_{\theta z}^{(2)}}{\partial \theta} + \frac{\partial \sigma_{zz}^{(2)}}{\partial z} + [\![\sigma_{rz}]\!] = 0 \end{aligned} \tag{8}$$

where $[\![\{\cdot\}]\!] = \{\cdot\}^{+} - \{\cdot\}^{-} = \{\cdot\}^{(0)} - \{\cdot\}^{(1)}$. Similarly, the continuity of the displacements between the inhomogeneities and the matrix holds at the interface $r = a$:

$$\mathbf{u}^{(1)}(a, \theta, z) = \mathbf{u}^{(0)}(a, \theta, z) \tag{9}$$

3 Isogeometric homogenization enhanced with surface elasticity

The isogeometric homogenization technique proposed recently by the present authors [35] focuses on the homogenization of unit cell embedding two- or three-dimensional inhomogeneities. The critical assumption is based on the periodicity of microstructures and asymptotic expansion of the displacements, stresses, and strains due to the large-scale separation between the size and spacing of the underlying heterogeneities and the homogenized materials dimensions. In what follows, the IGH technique incorporating the surface effect for nanocomposites is presented in detail.

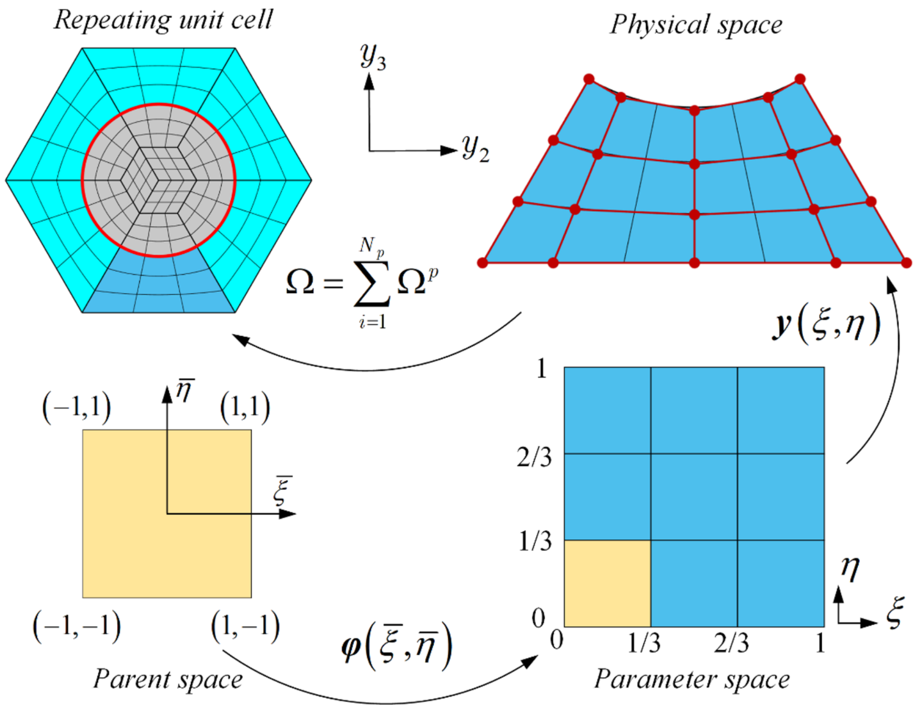

Fig. 2 Illustration of discretization of multiple conforming NURBS patches for hexagonal unit cell. The unit cell is obtained by mapping a square from the parent domain to the physical domain through the parametric domain. The red dots denote the distribution of the control points

3.1 NURBS surfaces

As shown in Fig. 2, we focus on a basic repeating unit cell. To represent the entire heterogeneous solids replicated in the two-dimensional space, periodic constants are considered at the unit cell boundary. This unit cell is then subdivided into a number of interconnected NURBS patches.

A NURBS curve can be created by the combination of control points and the univariate nonuniform rational B-spline (NURBS) basis functions. The B-spline basis functions are defined over a nondecreasing knot vector $\Xi = \left\{\xi_1, \xi_2, \xi_3, \ldots, \xi_{n+p+1}\right\}$ and can be obtained by using a recursive formula. The subscript n indicates the number of basis functions and p denotes the degree of functions. Mathematically, a series of B-spline basis functions can be written as, [36]:

$$N_{i,p}(\xi) = \begin{cases} 1, & \xi_i \le \xi < \xi_{i+1}, \\ 0, & \text{otherwise}, \end{cases} \tag{10}$$

for $p = 0$, and

$$N_{i,p}(\xi) = \frac{\xi - \xi_i}{\xi_{i+p} - \xi_i} N_{i,p-1}(\xi) + \frac{\xi_{i+p+1} - \xi}{\xi_{i+p+1} - \xi_{i+1}} N_{i+1,p-1}(\xi), \tag{11}$$

for $p > 0$. It can be noticed that the B-spline functions are piece-wise polynomial functions from the above definition. Generally, the first $p + 1$ and last $p + 1$ knots are set to be equal to obtain the interpolatory properties at the ends of NURBS geometries. The valid parametric domain for the i-th basis function is $[\xi_i, \xi_{i+p+1}]$. The continuities of a NURBS curve are C^∞ between adjacent knots and $C^{p-\alpha}$ at inner knots, where α denotes the multiplicity of the related knots.

Assume that Ξ_1 and Ξ_2 indicate the knot vectors defined along ξ and η directions, a NURBS surface is defined by

$$\boldsymbol{y}(\xi,\eta) = \sum_{A=1}^{nm} \boldsymbol{P}_A R_A(\xi,\eta), \quad R_A(\xi,\eta) = \frac{w_A N_A(\xi,\eta)}{\sum_{B=1}^{nm} w_B N_B(\xi,\eta)} \tag{12}$$

where $\boldsymbol{P}_A$ is the coordinate vector, and w_A is the weight of the A-th control point. R_A is the bivariate NURBS basis function, which can be calculated from the related univariate B-spline basis functions. The number of control points in two directions is n and m. The subscripts A and B indicate the index of control points, written as $A = n(j-1)+i$ and $B = n(l-1)+k$. The quad-like mesh constituted by knot lines is called IGH mesh, and each face corresponds to an IGH element, which will be further utilized for integral calculation based on the classical Gauss quadrature scheme.

3.2 Formulation of isogeometric homogenization incorporating surface elasticity theory

The isogeometric homogenization method is derived under the zeroth-order homogenization framework [37–40]. In this framework, the displacement fields are expressed in terms of dual-scale expansion involving macro- and microscopic contributions as follows:

$$\mathbf{u}^{(q)}(\mathbf{x},\mathbf{y}) = \bar{\boldsymbol{\varepsilon}} \cdot \mathbf{x} + \mathbf{u}'^{(q)}(\mathbf{y}) \tag{13}$$

In the above equation, $\bar{\boldsymbol{\varepsilon}}$ denotes the applied strains applied in the global coordinates. $\mathbf{u}'^{(q)}(\mathbf{y})$ denotes the fluctuating displacements, which are periodic functions on the local coordinate system $\mathbf{y}$. They are approximated in terms of NURBS-based interpolation functions $R_A^{(q)}(\xi,\ \eta)$ and the fluctuating displacements at the control points $\mathbf{u}_A'^{(q)}(\mathbf{y})$:

$$\mathbf{u}'^{(q)}(\mathbf{y}) = \sum_{A=1}^{mn} \mathbf{u}_A'^{(q)}(\mathbf{y}) \cdot R_A^{(q)}(\xi,\eta) \tag{14}$$

where $\mathbf{u}'^{(q)} = \left[u_1',\ u_2',\ u_3'\right]^{\mathrm{T}(q)}$, $\mathbf{u}_A'^{(q)} = \left[u_{1,A}'^{(q)},\ u_{2,A}'^{(q)},\ u_{3,A}'^{(q)}\right]^{\mathrm{T}}$. Substituting Eq. (13) into Eq. (2) yields the strain field in the following form:

$$\boldsymbol{\varepsilon}^{(q)} = \bar{\boldsymbol{\varepsilon}} + \boldsymbol{\varepsilon}'^{(q)} = \bar{\boldsymbol{\varepsilon}} + \frac{1}{2}\left(\nabla\mathbf{u}^{(q)} + \nabla\mathbf{u}^{\mathrm{T}(q)}\right) \tag{15}$$

In the above equation, $\boldsymbol{\varepsilon}'^{(q)}$ represents the fluctuating strain vector, which can be written as:

$$\boldsymbol{\varepsilon}'^{(q)}(\mathbf{y}) = \mathbf{B}^{(q)}\mathbf{U}'^{(q)} \tag{16}$$

where $\boldsymbol{\varepsilon}'^{(q)} = \left[\varepsilon_{11}',\ \varepsilon_{22}',\ \varepsilon_{33}',\ 2\varepsilon_{23}',\ 2\varepsilon_{13}',\ 2\varepsilon_{12}'\right]^{\mathrm{T}(q)}$, $\mathbf{U}'^{(q)} = \left[\mathbf{u}_1',\ \ldots,\ \mathbf{u}_A',\ \ldots,\ \mathbf{u}_{nm}'\right]^{(q)}$. $\mathbf{B}^{(q)}$ denotes the fluctuating strains and displacement matrix, which can be computed as follows:

$$\mathbf{B}^{(q)} = \left[\mathbf{B}_1^{(q)},\ \ldots\mathbf{B}_A^{(q)},\ \ldots\mathbf{B}_{nm}^{(q)}\right]$$

$$\mathbf{B}_A^{(q)} = \begin{bmatrix} R_{A,y_1} & 0 & 0 & 0 & R_{A,y_3} & R_{A,y_2} \\ 0 & R_{A,y_2} & 0 & R_{A,y_3} & 0 & R_{A,y_1} \\ 0 & 0 & R_{A,y_3} & R_{A,y_2} & R_{A,y_1} & 0 \end{bmatrix}^{(q)\mathrm{T}}$$

In order to proceed with the weak form formulation of a unit cell problem, it is crucial to represent stress, strain, and displacement vectors and stiffness tensor of the energetic surface, namely, Eqs. (4)–(6), in Cartesian coordinates. Toward this end, we first relate the axes in the Cartesian coordinates $(x_1,\ x_2,\ x_3)$ to those in the cylindrical coordinates $(z,\ r,\ \theta)$ via the following equations:

$$x_1 = z,\ x_2 = r\cos\theta,\ x_3 = r\sin\theta \tag{17}$$

Thus, the stress and strain vectors in Voigt notation undergo a transformation when transitioning between the cylindrical (denoted by the tilde symbol) and Cartesian coordinate systems, as follows:

$$\begin{gathered} \tilde{\boldsymbol{\varepsilon}} = \mathbf{Q}_\varepsilon \cdot \boldsymbol{\varepsilon},\ \tilde{\boldsymbol{\sigma}} = \mathbf{Q}_\sigma \cdot \boldsymbol{\sigma}, \\ \boldsymbol{\varepsilon} = \mathbf{Q}_\sigma^{\mathrm{T}} \cdot \tilde{\boldsymbol{\varepsilon}},\ \boldsymbol{\sigma} = \mathbf{Q}_\varepsilon^{\mathrm{T}} \cdot \tilde{\boldsymbol{\sigma}} \end{gathered} \tag{18}$$

where $\mathbf{Q}_\varepsilon$ and $\mathbf{Q}_\sigma$ denote proper fourth-order rotators [41]:

$$\mathbf{Q}_\varepsilon = \begin{bmatrix} 1 & 0 & 0 & 0 & 0 & 0 \\ 0 & \cos^2\theta & \sin^2\theta & \frac{1}{2}\sin 2\theta & 0 & 0 \\ 0 & \sin^2\theta & \cos^2\theta & -\frac{1}{2}\sin 2\theta & 0 & 0 \\ 0 & -\sin 2\theta & \sin 2\theta & \cos 2\theta & 0 & 0 \\ 0 & 0 & 0 & 0 & \cos\theta & -\sin\theta \\ 0 & 0 & 0 & 0 & \sin\theta & \cos\theta \end{bmatrix} \tag{19}$$

$$\mathbf{Q}_\sigma = \begin{bmatrix} 1 & 0 & 0 & 0 & 0 & 0 \\ 0 & \cos^2\theta & \sin^2\theta & \sin 2\theta & 0 & 0 \\ 0 & \sin^2\theta & \cos^2\theta & -\sin 2\theta & 0 & 0 \\ 0 & -\frac{1}{2}\sin 2\theta & \frac{1}{2}\sin 2\theta & \cos 2\theta & 0 & 0 \\ 0 & 0 & 0 & 0 & \cos\theta & -\sin\theta \\ 0 & 0 & 0 & 0 & \sin\theta & \cos\theta \end{bmatrix} \tag{20}$$

With the help of the above rotation matrices, the surface stiffness tensor in the cylindrical and Cartesian coordinates can be related via:

$$\mathbf{C}^{(2)} = \mathbf{Q}_\varepsilon^{\mathrm{T}} \cdot \tilde{\mathbf{C}}^{(2)} \cdot \mathbf{Q}_\varepsilon \tag{21}$$

We note that surface stiffness tensor Eq. (5) needs to be properly expanded by adding the zero terms in order to have the same dimension (6 × 6) as the rotation matrix.

The equilibrium equations shown in Eqs. (7) and (8) are solved using the isogeometric analysis. The weak form representation of the overall potential energy function Π of the composites is comprised of the strain energy density originating from the bulk U^b materials and energetic surface U^s, along with the external work W as follows:

$$\Pi = U^b + U^s - W = \frac{1}{2}\int_V \left(\boldsymbol{\sigma}^{\mathrm{T}} \cdot \boldsymbol{\varepsilon}\right)\mathrm{d}V + \frac{1}{2}\int_S \left(\boldsymbol{\sigma}^{(2)\mathrm{T}} \cdot \boldsymbol{\varepsilon}^{(2)}\right)\mathrm{d}S - \bar{\boldsymbol{\sigma}} \cdot \bar{\boldsymbol{\varepsilon}} \cdot V \tag{22}$$

In the above equations, $\bar{\boldsymbol{\sigma}}$ represent the volume-averaged stresses defined in the sequel. V denotes the unit cell volume. Substituting the strains, Eq. (15), and stresses, Eqs. (1) and (4) into Eq. (22), in the Cartesian coordinates, yields the potential energy function that is written in terms of surface and bulk stiffness tensors, the fluctuating control point displacements $\mathbf{U}'^{(q)}$, the strain–displacement matrix $\mathbf{B}^{(q)}$, and macroscopic strains and stresses (not shown). The local system of equations is obtained by taking the partial derivatives $\partial\Pi/\partial\mathbf{U}' = \mathbf{0}$:

$$\left\{\mathbf{k}^b + \mathbf{k}^s\right\}^{(q)} \mathbf{U}'^{(q)} = \left\{\mathbf{f}^b + \mathbf{f}^s\right\}^{(q)} \tag{23}$$

In the above equation, the superscripts b and s indicate the bulk and surface stiffness matrices and force vectors, respectively, with:

$$\begin{aligned} \mathbf{k}^b &= \int_V \mathbf{B}^{\mathrm{T}} \cdot \mathbf{C}^{(0,1)} \cdot \mathbf{B}\mathrm{d}V,\ \mathbf{k}^s = \int_S \mathbf{B}^{\mathrm{T}} \cdot \mathbf{C}^{(2)} \cdot \mathbf{B}\mathrm{d}S \\ \mathbf{f}^b &= -\left(\int_V \mathbf{B}^{\mathrm{T}} \cdot \mathbf{C}^{(0,1)}\mathrm{d}V\right)\bar{\boldsymbol{\varepsilon}},\ \mathbf{f}^s = -\left(\int_S \mathbf{B}^{\mathrm{T}} \cdot \mathbf{C}^{(2)}\mathrm{d}S\right)\bar{\boldsymbol{\varepsilon}} \end{aligned} \tag{24}$$

Assembly of Eq. (23) by enforcing the continuity and periodicity conditions of fluctuating control point displacements yields a final system of equations for determining the fluctuating displacements in the local coordinates:

$$\left\{\mathbf{K}^b + \mathbf{K}^s\right\}\mathbf{U}' = \mathbf{F}^b + \mathbf{F}^s \tag{25}$$

It is evident that Eq. (25) simplifies to the classical computational homogenization when the interfaces are disregarded. It should be noted that the periodicity conditions are applied directly during the assembly process of the local system of equations. This is achieved by consistently numbering the control points along the opposite unit cell edges.

To generate one column of homogenized stiffness tensor of the unit cell $\mathbf{C}^*$, the global system of equations, Eq. (25), is solved by sequentially applying one unit macroscopic strain component at a time, with other strain components kept as zeros. In the presence of surface stresses, the homogenized stresses of the unit cell for the six loading cases can be obtained by volume-averaging of the stresses in the bulk materials and energetic surface as follows:

$$\overline{\boldsymbol{\sigma}} = \frac{1}{V}\int_V \boldsymbol{\sigma}^{(0,1)}\mathrm{d}V + \frac{1}{V}\int_S \boldsymbol{\sigma}^{(2)}\mathrm{d}S \tag{26}$$

It is worth pointing out that when cylindrical inhomogeneities are distributed randomly or arranged periodically in a hexagonal array, the resulting macroscopic properties exhibit transversely isotropic characteristics, characterized by five elastic constants, k^*, l^*, n^*, m^* and p^*.

4 Verifications

In this section, the accuracy of the extended IGH framework enriched with energetic surfaces is validated against available solutions in the literature. It is important to point out that the interfacial elastic constants are typically derived from molecular dynamics simulations specific to a particular atomic lattice. Nevertheless, such data are limited in availability, and energetic surface moduli associated with porosity boundaries have primarily been reported for lattices composed of aluminium and silicon. Therefore, in the following simulations, we focus on aluminium nanoporous arrays where the surface effect prevails. The cylindrical porosities are distributed periodically in the hexagonal and square manner in $x_2 - x_3$ plane. The bulk aluminium Young's modulus and Poisson's ratio are: $E^{(0)} = 90.2\text{GPa}$, $v^{(0)} = 0.3$, respectively. We employ two distinct sets of surface elastic constants, resulting in significantly varied stress distributions and homogenized moduli as the pore dimensions decrease [42]. For the surface labelled as Surface A, $\lambda^{(2)} = 3.4821\text{N/m}$, $\mu^{(2)} = -6.2178\text{N/m}$ and for the surface labelled as Surface B, $\lambda^{(2)} = 6.842\text{N/m}$, $\mu^{(2)} = -0.3755\text{N/m}$. These surface constants yield the softening and stiffening behaviour of such materials at small fiber/pore radii when compared to the classical results without surface effect, respectively. The numerical implementation of IGH is developed on our open-source framework NLIGA [33, 43].

4.1 Stress concentration factor under far-field loading

Precise characterization of the localized stress fields and the concurrent identification of maximum stress points in the vicinity of pores are pivotal for understanding the failure modes in nanoporous materials. In this subsection, we first consider an infinite plate embedding circular porosity in the centre, where the surface elasticity model is considered. The plate is subjected to uniform in-plane normal stress $\sigma_{22}^{\infty} = \sigma_{33}^{\infty} = \sigma_o$ and transverse shear stress $\sigma_{22}^{\infty} = -\sigma_{33}^{\infty} = \sigma_o$ at infinity, respectively, which is the so-called extended Kirsch problem. The stress fields at the interface may be evaluated to produce the hoop stress concentration factors (SCF). The explicit expressions for hoop stress distributions are first obtained by Chen et al. [17], which are formulated in relation to surface and matrix moduli, as well as the radius of the pore, and are presented below:

$$\left.\frac{\sigma_{\theta\theta}^{(0)}}{\sigma_0}\right|_{r=a} = \frac{2 + \frac{1}{2a}\left(\lambda^{(2)} + 2\mu^{(2)}\right)\left(\frac{1}{\mu^{(0)}} - \frac{1}{k^{(0)}}\right)}{1 + \frac{1}{2a\mu^{(0)}}\left(\lambda^{(2)} + 2\mu^{(2)}\right)},\ \sigma_{22}^{\infty} = \sigma_{33}^{\infty} = \sigma_o \tag{27}$$

$$\left.\frac{\sigma_{\theta\theta}^{(0)}}{\sigma_0}\right|_{r=a} = \frac{4 + \frac{1}{a}\left(\lambda^{(2)} + 2\mu^{(2)}\right)\left(\frac{1}{\mu^{(0)}} - \frac{1}{k^{(0)}}\right)}{1 + \frac{1}{2a}\left(\lambda^{(2)} + 2\mu^{(2)}\right)\left(\frac{2}{\mu^{(0)}} + \frac{1}{k^{(0)}}\right)}\cos 2\theta,\ \sigma_{22}^{\infty} = -\sigma_{33}^{\infty} = \sigma_o \tag{28}$$

Evidently, the aforementioned equations simplify to the classical Kirsch problem in the absence of surface elasticity, either when the pore radius approaches infinity or when the surface moduli decrease significantly.

To mimic the Kirsch problem with the presented IGH framework, we consider a square unit cell containing 1% of the pore volume fraction. In such a case, the effect of periodic boundary conditions on the local stress concentration is negligible in the vicinity of the interface. The far-field loadings for in-plane normal and shear loadings are replaced by $\overline{\sigma}_{22} = \overline{\sigma}_{33} = \sigma_o$ and $\overline{\sigma}_{22} = -\overline{\sigma}_{33} = \sigma_o$, respectively. As illustrated in Fig. 3, under transverse loading, the presented IGH framework shows excellent accordance with Chen's results in predicting the hoop stress concentration factors for the pore radii within a range where the impact of surface elasticity becomes evident. The slight discrepancy noticed in Fig. 3 can be attributed to variances in boundary conditions. In the extended Kirsch problem, far-field loads are employed in the elasticity solution, whereas the IGH framework relies on the rigorous periodicity of microstructures.

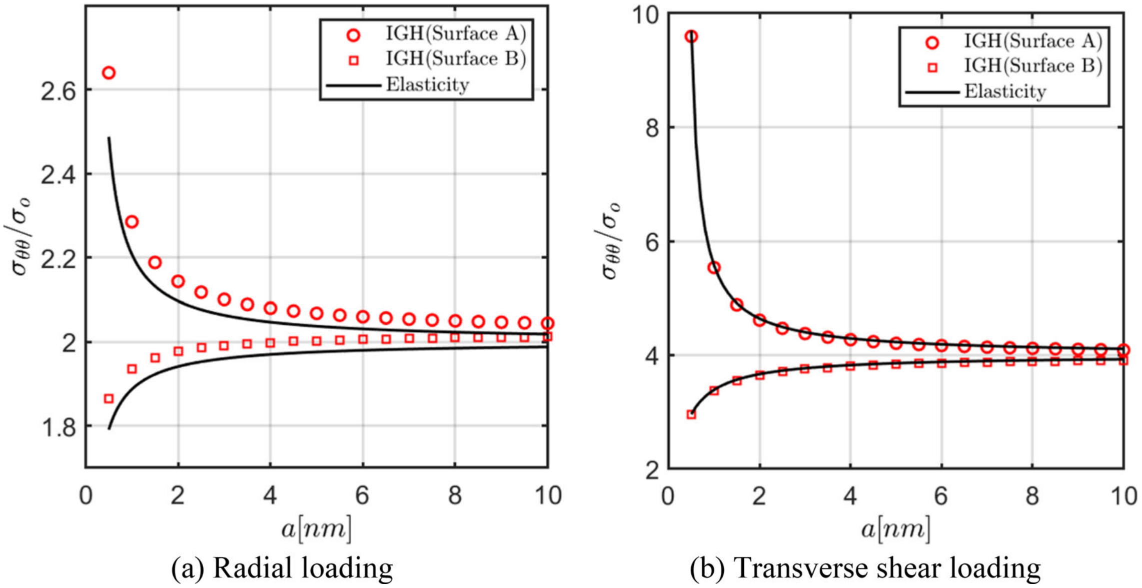

(a) Radial loading

(b) Transverse shear loading

Fig. 3 The stress concentration factors at the pore boundary: (**a**) radial loading $\overline{\sigma}_{22} = \overline{\sigma}_{33} = \sigma_o$; (**b**) transverse shear loading $\overline{\sigma}_{22} = -\overline{\sigma}_{33} = \sigma_o$

4.2 Homogenized moduli

To further demonstrate the modelling and predictive performances of the proposed micromechanics framework, the homogenized moduli of nanoporous materials with different pore volume fractions and radii are computed and compared with the Mori–Tanaka scheme [15], the locally exact homogenization theory [23], the equivalent inhomogeneity technique [31], and the finite-volume direct averaging micromechanics (FVDAM) [25] and the finite-element predictions [28].

Figure 4 shows a hexagonal repeating unit cell containing six conforming NURBS patches that are employed in the IGH simulations. Each patch is further discretized into 16 × 16 elements, yielding 1536 elements in total. Figure 5 shows the discrepancies between the axisymmetric moduli n^*, k^* and the axial and transverse shear moduli p^*, m^* computed using the Mori–Tanaka and LEHT methods with the presented IGH micromechanics technique. This comparison is presented as a function of pore volume fraction, and it includes two variations of surface properties and pore radii ($a = 5$ nm and $a = 20$ nm). To clearly demonstrate the effect of the energetic surface on the effective composite moduli, all results are normalized based on their corresponding classical values without surface elasticity. It is noted that, regardless of the pore radii and surface types considered, there is a notable alignment among the results obtained using the three approaches for the axisymmetric n^*, k^* and axial shear p^* moduli. While the IGH and LEHT theories provide indistinguishable predictions for the transverse shear moduli m^*, the MT method significantly underestimates these values, with the differences between the MT and IGH/LEHT increasing with increasing pore volume fractions and decreasing pore radii. The exceptional consistency between the IGH and LEHT predictions can be attributed to the fact that both methods account explicitly for pore interaction which becomes important at high pore volume fractions. In contrast, the classical MT micromechanics technique incorporates this interaction only in an averaged sense.

Figure 6 compares the IGH and LEHT predictions of the plane strain bulk moduli k^* and transverse shear moduli m^* with those obtained based on the EIT prediction of Mogilevskaya et al. [31], as a function of pore volume fractions. The EIT is a homogenization approach rooted in elasticity principles. It entails solving for the displacement and stress fields within both the matrix and the cluster of fibers. We focus on only the pore radius of $a = 5$ nm due to the more significant surface effect. As observed, the IGH and LEHT predictions correlate very well with the EIT results over the considered range of pore volume fractions.

Figure 7 presents the comparison of the LEHT and FVDAM predictions of the axisymmetric moduli n^*, k^* and the axial and transverse shear moduli p^*, m^* with the presented IGH micromechanics technique as a function of pore radii. The pore volume fraction is kept as a constant at $V_f = 30\%$. The FVADM is a semi-analytical and finite-volume-based unit cell solution that satisfies strong form equilibrium equations and periodic displacements and tractions, albeit at a volume- or surface-averaged sense. Once again, there is a

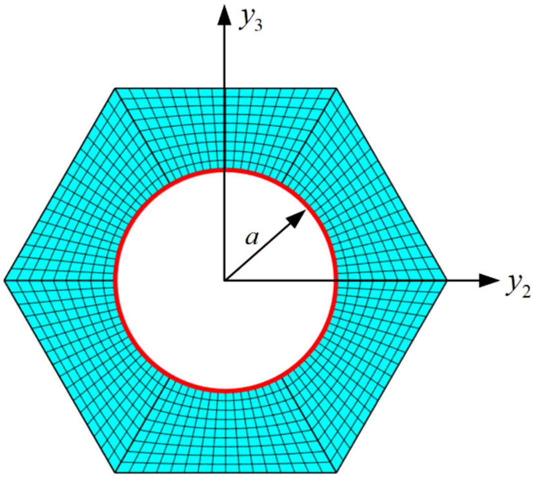

Fig. 4 Discretization of a hexagonal unit cell with the Gurtin–Murdoch interface with six patches in the presented IGH method

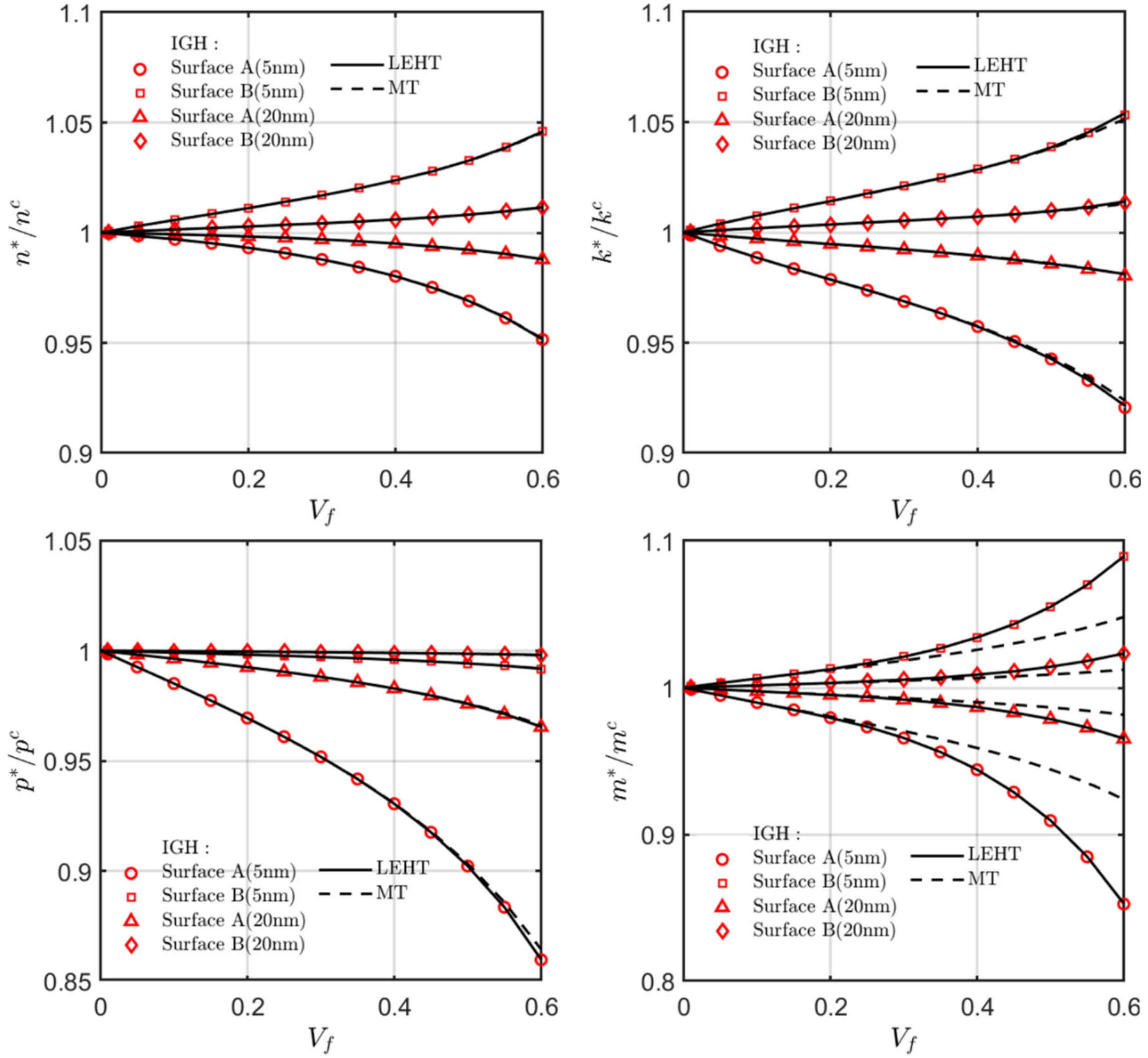

Fig. 5 Normalized effective axisymmetric and shear moduli of a hexagonal array of cylindrical porosity. Comparison with the LETH and classical MT micromechanics predictions

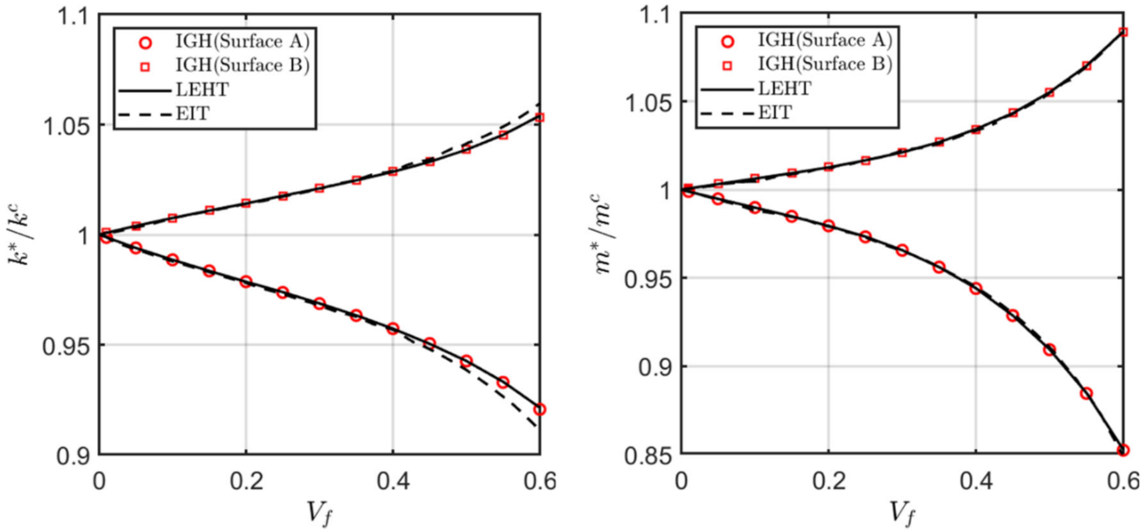

Fig. 6 Normalized effective plane strain bulk and transverse shear moduli of hexagonal array of cylindrical porosity with the pore radius $a = 5$ nm. Comparison with the EIT homogenization

remarkable correlation between the IGH results and the benchmark solutions. It should be noted that both the LEHT and EIT techniques are elasticity-theory-based solutions. Currently, both techniques are limited to the modelling of unidirectional composites with cylindrical porosity, while the present technique can be easily extended to the three-dimensional domain to accommodate arbitrarily shaped inhomogeneities. The FVDAM employs the volume/surface averaging solution of the unit cell problem, based on the finite-volume theory. The surface equilibrium equations (or the so-called Young–Laplace conditions) are implemented through the finite-difference method, which is difficult to extend to the three-dimensional domain.

In the last example, comparison of the IGH predictions of the plane strain bulk moduli and transverse shear moduli with conventional finite-element results is conducted in Fig. 9. The latter was performed by Gao et al. [28] using ANSYS based on a square array of cylindrical porosity with 30% volume content. The IGH mesh with four NURBS patches employed in the study is shown in Fig. 8. As depicted in Fig. 9, minor discrepancies can be noted for plane strain bulk moduli among Gao's reported results with the predictions from LEHT and the IGH techniques. These differences tend to decrease as the pore radius increases. We also note that when it comes to the transverse shear moduli, more significant distinctions are observed between Gao's results and those from the IGH/LEHT methods, particularly within the smaller pore radius range. It should be emphasized that Gao et al. [28] mentioned that the ANSYS software encounters convergence and stability issues when the pore radius is below 2 nm. The IGH technique does not yield such a problem in the examined pore radius and volume fraction range.

4.3 Local stress fields

Having examined the predictive capabilities of the proposed micromechanics technique in generating the macroscopic properties of nanoporous materials, we proceed to investigate the energetic surface effect on the local stress field distributions under different loading scenarios. Accurate local stress field predictions are crucial for the design of durable and sustainable nanoporous structures with specific applications. The proposed IGH technique is highly suitable for predicting the full stress fields in nanoporous media with surface elasticity due to its stability, accuracy, and the ability to explicitly consideration of microstructures. Conversely, the classical micromechanics method, such as MT, can provide only an average stress value per phase. It cannot be utilized to predict the adjacent pore interaction, which is important at high pore contents.

Figures 10and11 present differences in transverse shear stress $\sigma_{23}(y_2,\ y_3)$ and axial shear stress $\sigma_{12}(y_2,\ y_3)$ for hexagonal unit cells for the type A surface at two different pore radii $a = 1$ nm and $a = 10$ nm. These stresses are evaluated under transverse shear loading $\overline{\varepsilon}_{23} = 0.1\%$ and axial shear loading $\overline{\varepsilon}_{12} = 0.1\%$, respectively, by the IGH and LEHT techniques. We have chosen 50% high volume fraction due to the pronounced pore–pore interaction. Notably, surface A produces substantially higher stress concentrations in the vicinity of

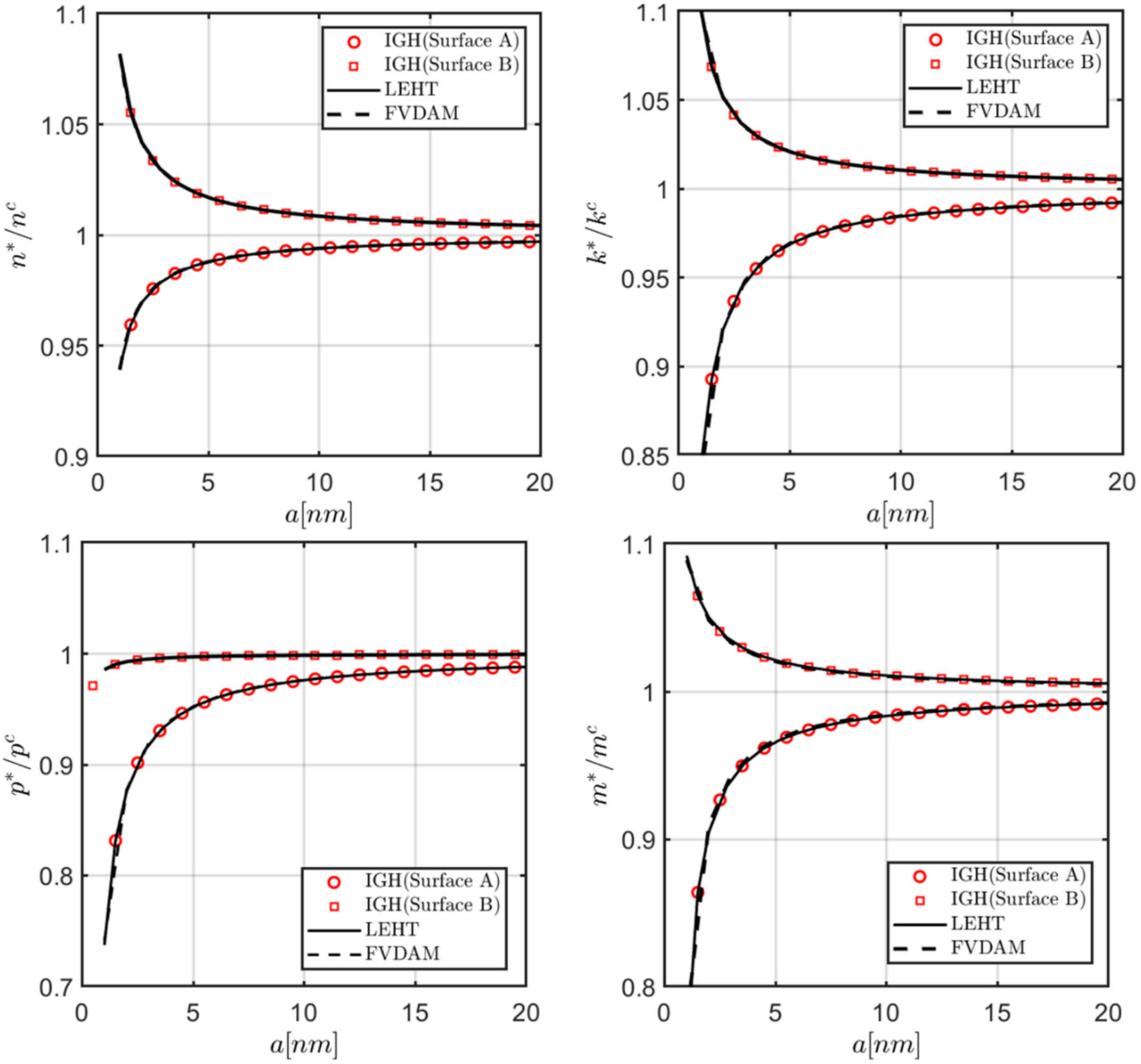

Fig. 7 Normalized axisymmetric and shear moduli of a hexagonal array of cylindrical porosity with 30% volume fraction. Comparison with the IGH predictions with benchmark solutions

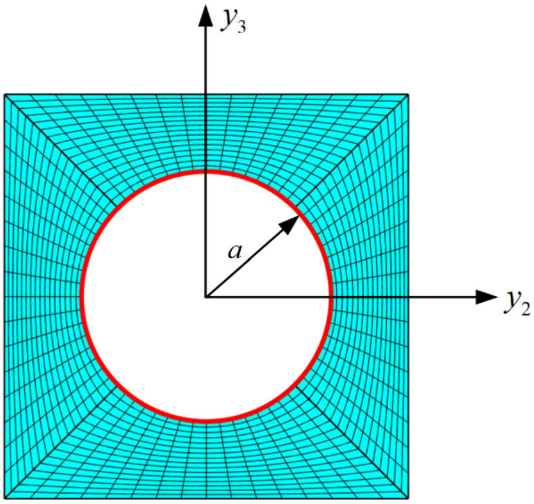

Fig. 8 Discretization of the square unit cell with the Gurtin–Murdoch interface with four patches in the presented IGH method

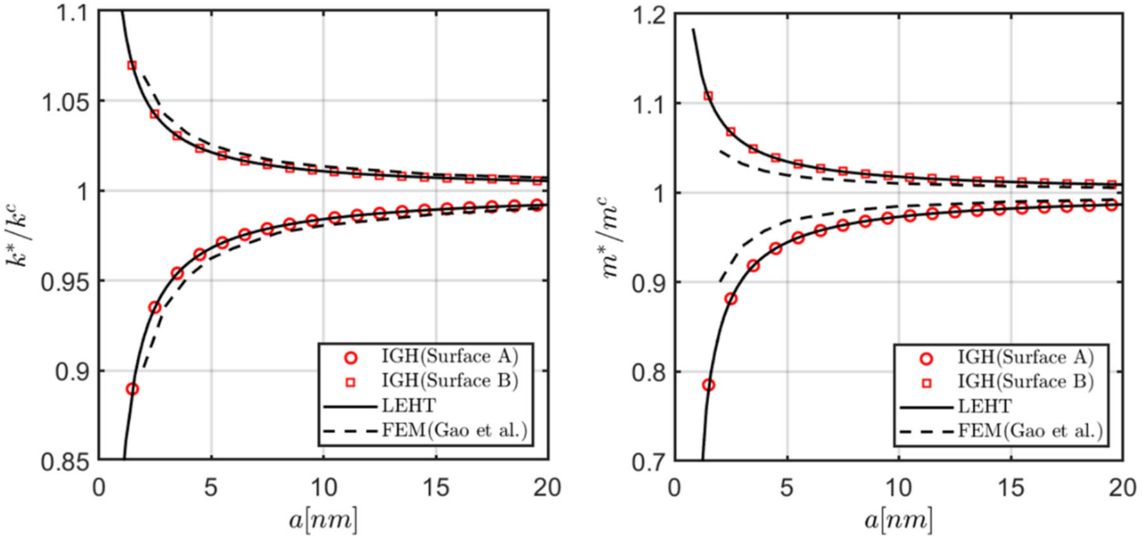

Fig. 9 Normalized plane strain bulk and shear moduli of a square array of cylindrical porosity for the 30% of pore volume fraction

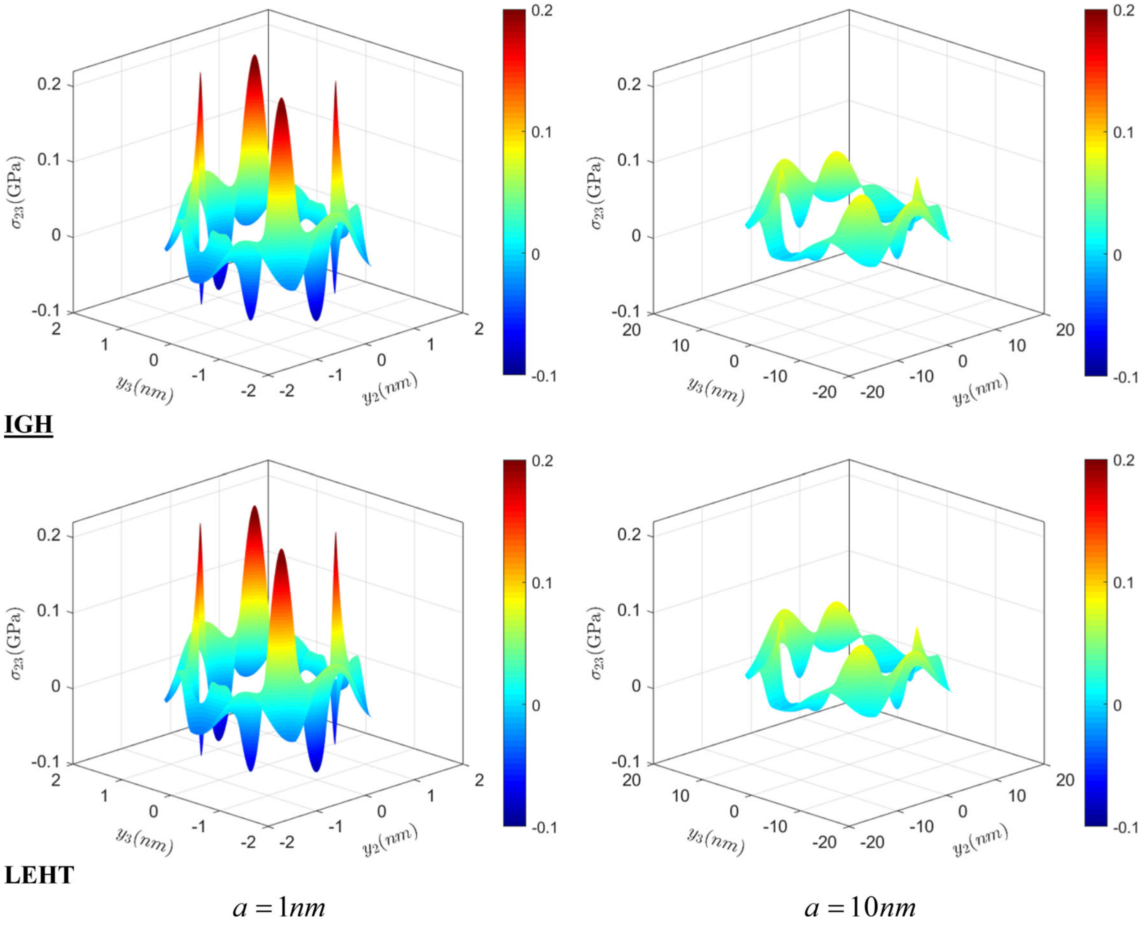

Fig. 10 Transverse shear stress fields σ_{23} in the unit cell with 50% porosity volume fraction subjected to transverse shear loading $\bar{\varepsilon}_{23} = 0.1\%$, predicted by the IGH and LEHT homogenization of hexagonal arrays for 1 nm and 10 nm pore radii with surface A properties

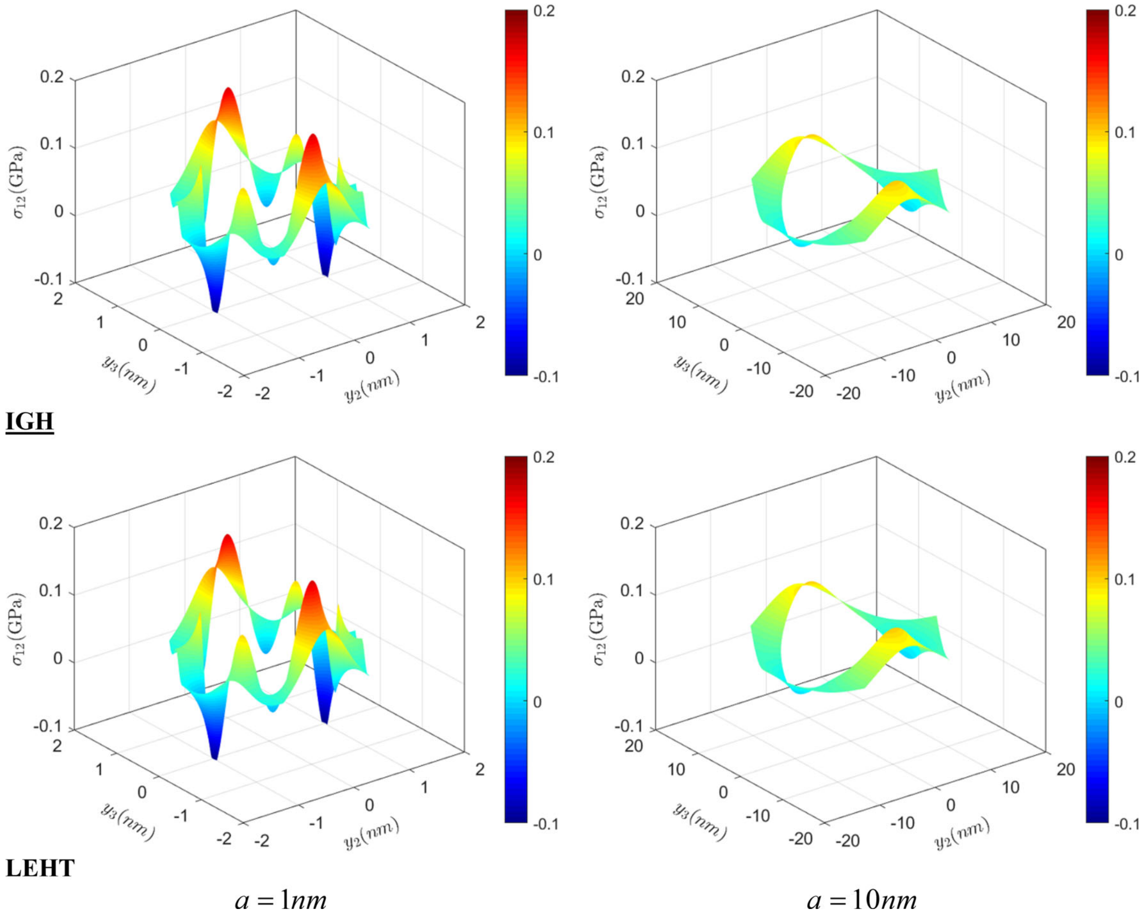

Fig. 11 Axial shear stress fields σ_{12} in the unit cell with 50% porosity volume fraction subjected to transverse shear loading $\overline{\varepsilon}_{12} = 0.1\%$, predicted by the IGH and LEHT homogenization of hexagonal arrays for 1 nm and 10 nm pore radii with surface A properties

the pore boundary at the pore radius of $a = 1$ nm than those at the pore radius of $a = 10$ nm. The stress field distributions obtained from both computational approaches are found to be virtually identical at the chosen pore radii and volume fraction. We highlight that the fundament difference between the IGH and LEHT unit cell problems lies in the fact that the LEHT unit cell solution relies on the strong form solution of the stress equilibrium equations in the bulk materials, with the Gurtin–Murdoch interface model introduced through the Young–Laplace equations. In contrast, the IGH approach relies on minimizing the total potential energy, and it integrates the Gurtin–Murdoch interface model by introducing supplementary surface energies linked to the elements along the boundaries of the pores.

We further examine the impact of unit cell type on the predicated transverse shear stresses under transverse shear loading $\overline{\varepsilon}_{23} = 0.1\%$. This analysis was performed with surface B properties at the pore radius $a = 1$ nm, as shown in Fig. 12. Once again, the correlations between the IGH and LEHT predictions with surface B properties are remarkable for the hexagonal and square arrays alike. The stress fields are substantially different for the two arrays, highlighting the important adjacent pore interactions with different microstructural arrays at the high pore volume content range.

5 Discussion

Micromechanics plays an important role in predicting not only the homogenized moduli but also local stress field distributions, and hence the damage evolution and ultimate failure of composite materials. The classical micromechanics methodologies, such as the MT technique, neglect the intricate interactions between different phases at intermediate- and high-volume fraction ranges; therefore, they are incapable of predicting

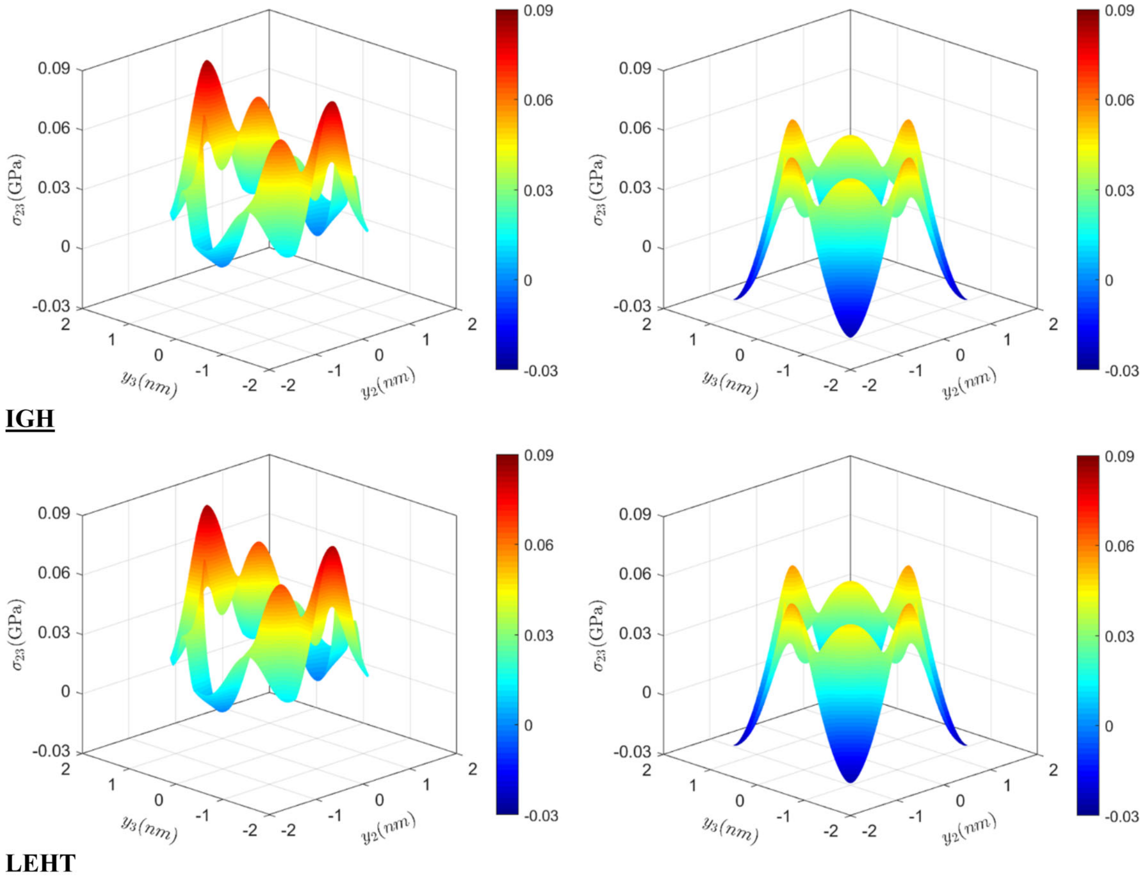

(a) Hexagonal array (b) Square array

Fig. 12 Transverse shear stress fields σ_{23} in the unit cell with 50% porosity volume fraction subjected to transverse shear loading $\bar{\varepsilon}_{23} = 0.1\%$, predicted by the IGH and LEHT homogenization of hexagonal and square array types

accurately the local stress field distributions, if not the homogenized moduli. In response to this limitation, full-field homogenization approaches requiring more sophisticated analytical or numerical treatments continue to emerge, with efficiency and accuracy of the local stress field reconstruction of major considerations. Presently, the analytical solutions for full-field homogenization theories are limited in their availability and the finite-element method remains the primary means of implementation in the literature [44, 45].

It is the objective of the present work to present a new finite-element framework for homogenization and localization of nanoporous composites via the isogeometric analysis technique. The proposed IGH technique directly employs the NURBS functions as shape functions, eliminating the need for the complex mesh discretization associated with the conventional FEM. More importantly, the proposed theory facilitates smoother and more accurate field approximations due to the satisfaction of higher-order continuity through the use of higher-order NURBS basis functions, without sacrificing the computational efficiency. This presents a substantial advantage over the conventional finite-element technique since the latter ensures only C^0 continuity conditions of displacement. In order to clearly demonstrate the advantages of the proposed technique over the classical finite-element homogenization scheme, we consider a hexagonal array of cylindrical porosity with 30% of pore volume fraction and surface A property, subjected to uniaxial strain loading by $\bar{\varepsilon}_{22} = 0.1\%$. As shown in Fig. 4, the unit cell is discretized into 96×9 elements in both IGH and conventional finite-element calculations. Figure 13 presents the comparison of the IGH-predicted transverse normal stress σ_{22} using the 2nd- and 4th-order NURBS basis functions with the corresponding results obtained from 4-noded and 8-noded finite elements. The pore radius is 1 nm. It should be noted that to represent a circular geometry accurately, it is necessary to employ NURBS basis functions of at least second order. As shown in Fig. 13, the transverse normal stress σ_{22} exhibits remarkable variation in the vicinity of the pore boundary due to the significant negative surface energies. The lower-order FEM Q4 predictions differ significantly from the proposed IGH

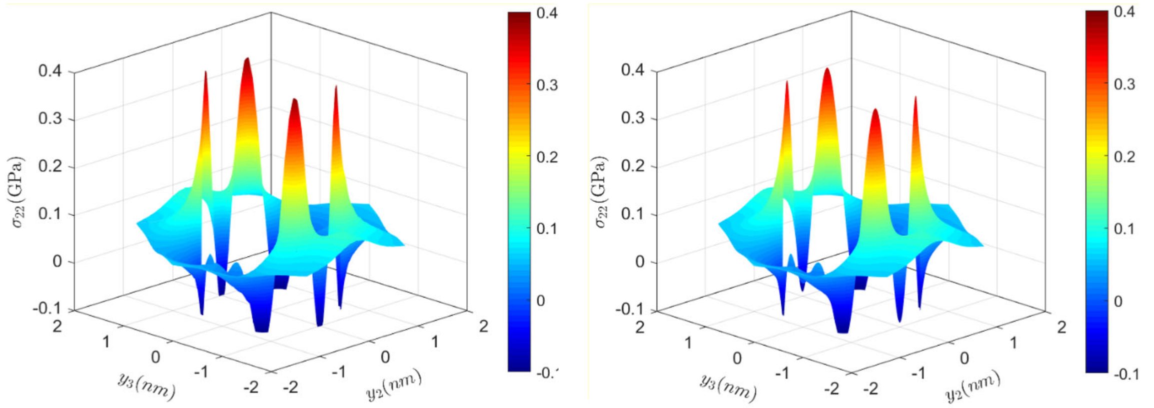

IGH- $p = q = 2$ IGH- $p = q = 4$

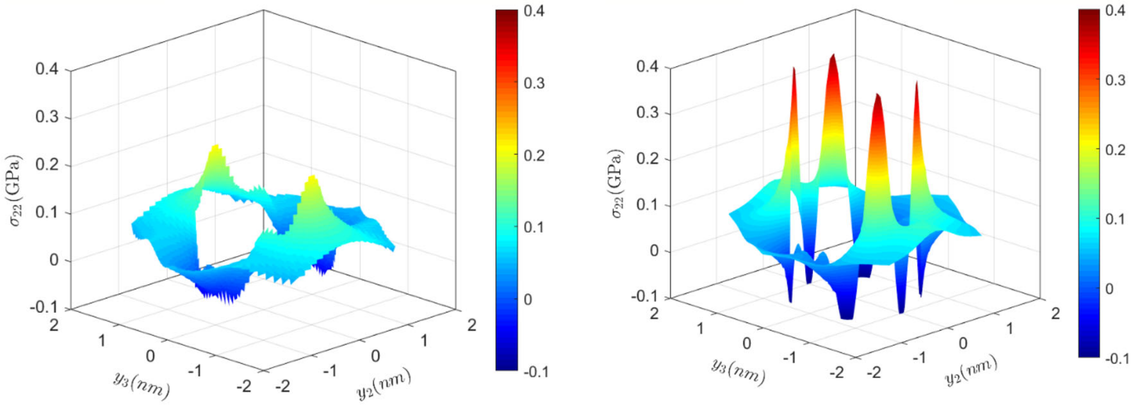

FEM-Q4 FEM-Q8

Fig. 13 Transverse normal stress fields σ_{22} in the unit cell with 1 nm pore radius subjected to transverse normal loading $\overline{\varepsilon}_{22} = 0.1\%$, predicted by the IGH and conventional finite-element techniques

and FEM Q8. In contrast, the IGH technique consistently produces nearly identical results to the 8-noded FEM, even when utilizing the 2nd-order NURBS basis function, showcasing the proposed method's ability to generate more robust and accurate solutions. Figure 14 shows the transverse normal stress σ_{22} distribution generated by the IGH and conventional FEM methods when the pore radius is increased to 2 nm. It is observed that the IGH technique provides smoother and more accurate stress distributions relative to the conventional FEM results.

Comparison of degrees of freedom (DOF) and execution times in an uncompiled MATLAB environment between the IGH and conventional FEM techniques is presented in Table 1. We note that the IGH with 2nd-order NURBS basis functions exhibits a similar number of DOF and execution times as the 4-noded FEM. In contrast, the IGH with fourth-order NURBS basis functions possesses fewer DOF and proves more efficient than the 8-noded FEM.

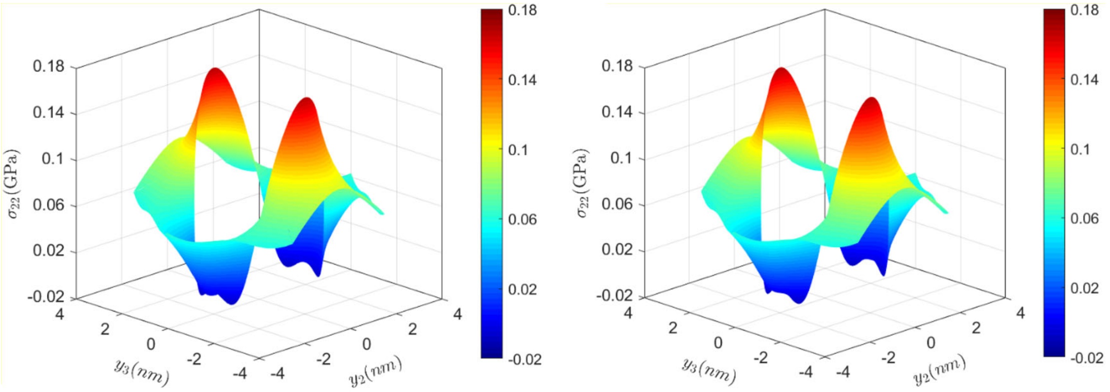

IGA- $p = q = 2$ IGA- $p = q = 4$

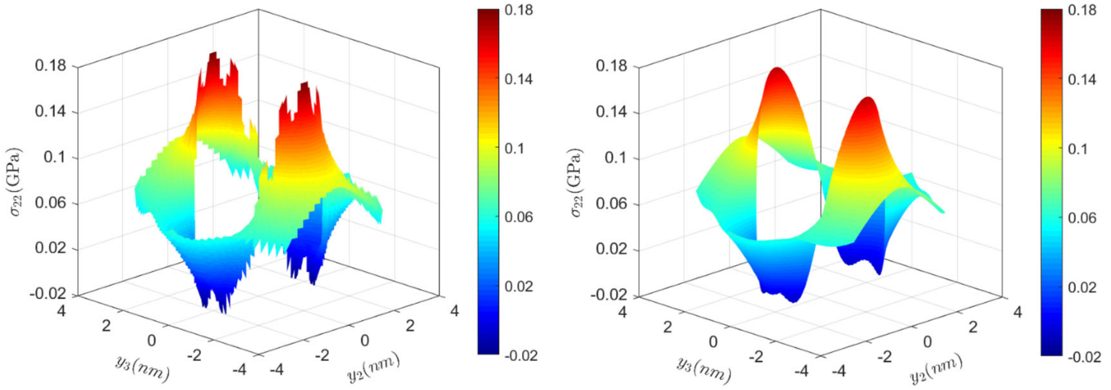

FEM-Q4 FEM-Q8

Fig. 14 Transverse normal stress fields σ_{22} in the unit cell with 2 nm pore radius subjected to transverse normal loading $\bar{\varepsilon}_{22} = 0.1\%$, predicted by the IGH and conventional finite-element techniques

Table 1 Comparison of DOF and execution times between the IGH and conventional FEM techniques

	IGH-$p = q = 2$	IGH-$p = q = 4$	FEM Q4	FEM Q8
DOF	3210	4272	2733	8061
Time (seconds)	2.62	9.16	1.141	11.06

6 Conclusions

In this contribution, the isogeometric homogenization framework has been further extended by adopting the Gurtin–Murdoch surface elasticity theory for predicting the macroscopic elastic moduli and local stress field in nanoporous composites. The presented method utilized a dual-scale representation of the displacement field within the repeating unit cell for periodic microstructures. In this approach, the local unit cell problem was solved under periodic boundary constraints. The Gurtin–Murdoch interface model was introduced into the proposed framework via supplementary surface energies linked to the elements along the boundaries of the pores. The formation and assembly of surface element stiffness matrices were carried out independently from the bulk materials while keeping the fundamental IGH framework unchanged. The surface-enriched IGH strategy was employed for predicting macroscopic effective moduli and local field variables to mechanical loading for hexagonal and square arrays of cylindrical porosity in an aluminium matrix. To validate its accuracy, the results were compared against exact elasticity solutions as well as finite-element and finite-volume simulations. The numerical examples presented in this manuscript demonstrate the developed model's accuracy, akin to the exact elasticity solution.

Acknowledgements Dr. Xiaoxiao Du gratefully acknowledges the financial support of National Natural Science Foundation of China (Project No 62102012) and Young Elite Scientists Sponsorship Program by CAST (Project No 2022QNRC001).

Declarations

Conflict of interest The authors declare that they have no known competing financial interests or personal relationships that could have appeared to influence the work reported in this paper.

References

1. Chatzigeorgiou, G., Meraghni, F., Javili, A.: Generalized interfacial energy and size effects in composites. J. Mech. Phys. Solids **106**, 257–282 (2018)
2. Firooz, S., Steinmann, P., Javili, A.: Homogenization of composites with extended general interfaces: comprehensive review and unified modeling. Appl. Mech. Rev. **73**, 040802 (2021)
3. Firooz, S., Chatzigeorgiou, G., Meraghni, F., Javili, A.: Homogenization accounting for size effects in particulate composites due to general interfaces. Mech. Mater. **139**, 103204 (2019)
4. Guinovart-Díaz, R., Rodríguez-Ramos, R., López-Realpozo, J.C., Bravo-Castillero, J., Otero, J.A., Sabina, F.J., et al.: Analysis of fibrous elastic composites with nonuniform imperfect adhesion. Acta Mech. **227**, 57–73 (2016)
5. Otero, J.A., Rodríguez-Ramos, R., Bravo-Castillero, J., Guinovart-Díaz, R., Sabina, F.J., Monsivais, G.: Semi-analytical method for computing effective properties in elastic composite under imperfect contact. Int. J. Solids Struct. **50**, 609–622 (2013)
6. Zhao, Z., Zhu, J., Chen, W.: Size-dependent vibrations and waves in piezoelectric nanostructures: a literature review. Int. J. Smart Nano Mater. **13**, 391–431 (2022)
7. Gurtin, M.E., Murdoch, A.I.: A continuum theory of elastic material surfaces. Arch. Ration. Mech. Anal. **57**, 291–323 (1975)
8. Gurtin, M.E., Murdoch, A.I.: Surface stress in solids. Int. J. Solids Struct. **14**, 431–440 (1978)
9. Chen, T., Chiu, M.-S., Weng, C.-N.: Derivation of the generalized Young-Laplace equation of curved interfaces in nanoscaled solids. J. Appl. Phys. **100**, 074308 (2006)
10. Barenblatt, G.I.: The formation of equilibrium cracks during brittle fracture General ideas and hypotheses Axially-symmetric cracks. J. Appl. Math. Mech. **23**, 622–636 (1959)
11. Barenblatt, G.I.: The mathematical theory of equilibrium cracks in brittle fracture. In: Dryden, H.L., von Kármán, T., Kuerti, G., van den Dungen, F.H., Howarth, L. (eds.) Advances in applied mechanics, pp. 55–129. Elsevier, Amsterdam (1962)
12. Needleman, A.: A continuum model for void nucleation by inclusion debonding. J. Appl. Mech. **54**, 525–531 (1987)
13. Benveniste, Y., Miloh, T.: Imperfect soft and stiff interfaces in two-dimensional elasticity. Mech. Mater. **33**, 309–323 (2001)
14. Benveniste, Y.: A general interface model for a three-dimensional curved thin anisotropic interphase between two anisotropic media. J. Mech. Phys. Solids **54**, 708–734 (2006)
15. Chen, Q., Wang, G., Pindera, M.-J.: Homogenization and localization of nanoporous composites—a critical review and new developments. Compos. B Eng. **155**, 329–368 (2018)
16. Mogilevskaya, S.G., Zemlyanova, A.Y., Kushch, V.I.: Fiber- and particle-reinforced composite materials with the gurtin-murdoch and steigmann-ogden surface energy endowed interfaces. Appl. Mech. Rev. **73**, 050801 (2021)
17. Chen, T., Dvorak, G.J., Yu, C.C.: Size-dependent elastic properties of unidirectional nano-composites with interface stresses. Acta Mech. **188**, 39–54 (2007)
18. Moshtaghin, A.F., Naghdabadi, R., Asghari, M.: Effects of surface residual stress and surface elasticity on the overall yield surfaces of nanoporous materials with cylindrical nanovoids. Mech. Mater. **51**, 74–87 (2012)
19. Kushch, V.I.: Atomistic vs. continuum models of nanoporous elastic solid: stress fields, size-dependent effective stiffness and surface constants. Mech. Mater. **166**, 104223 (2022)
20. Duan, H.L., Yi, X., Huang, Z.P., Wang, J.: A unified scheme for prediction of effective moduli of multiphase composites with interface effects. Part I: theoretical framework. Mech. Mater. **39**, 81–93 (2007)
21. Chen, Q., Chatzigeorgiou, G., Meraghni, F.: Extended mean-field homogenization of unidirectional piezoelectric nanocomposites with generalized Gurtin-Murdoch interfaces. Compos. Struct. **307**, 116639 (2023)
22. Duan, H.L., Wang, J., Huang, Z.P., Karihaloo, B.L.: Size-dependent effective elastic constants of solids containing nano-inhomogeneities with interface stress. J. Mech. Phys. Solids **53**, 1574–1596 (2005)
23. Wang, G., Chen, Q., He, Z., Pindera, M.-J.: Homogenized moduli and local stress fields of unidirectional nano-composites. Compos. B Eng. **138**, 265–277 (2018)
24. Chen, Q., Pindera, M.-J.: Homogenization and localization of elastic-plastic nanoporous materials with Gurtin-Murdoch interfaces: an assessment of computational approaches. Int. J. Plast. **124**, 42–70 (2020)
25. Chen, Q., Wang, G., Pindera, M.-J.: Finite-volume homogenization and localization of nanoporous materials with cylindrical voids. Part 1: theory and validation. Eur. J. Mech.-A/Solids **70**, 141–155 (2018)
26. Javili, A., Steinmann, P.: A finite element framework for continua with boundary energies. Part I: the two-dimensional case. Comput. Methods Appl. Mech. Eng. **198**, 2198–2208 (2009)
27. Chen, Q., Chatzigeorgiou, G., Meraghni, F., Javili, A.: Homogenization of size-dependent multiphysics behavior of nanostructured piezoelectric composites with energetic surfaces. Eur. J. Mech. A. Solids **96**, 104731 (2022)
28. Gao, W., Yu, S., Huang, G.: Finite element characterization of the size-dependent mechanical behaviour in nanosystems. Nanotechnology **17**, 1118–1122 (2006)
29. Tian, L., Rajapakse, R.: Finite element modelling of nanoscale inhomogeneities in an elastic matrix. Comput. Mater. Sci. **41**, 44–53 (2007)
30. Mogilevskaya, S.G., Crouch, S.L., Stolarski, H.K., Benusiglio, A.: Equivalent inhomogeneity method for evaluating the effective elastic properties of unidirectional multi-phase composites with surface/interface effects. Int. J. Solids Struct. **47**, 407–418 (2010)
31. Mogilevskaya, S.G., Crouch, S.L., La Grotta, A., Stolarski, H.K.: The effects of surface elasticity and surface tension on the transverse overall elastic behavior of unidirectional nano-composites. Compos. Sci. Technol. **70**, 427–434 (2010)

32. Hughes, T.J.R., Cottrell, J.A., Bazilevs, Y.: Isogeometric analysis: CAD, finite elements, NURBS, exact geometry and mesh refinement. Comput. Methods Appl. Mech. Eng. **194**, 4135–4195 (2005)
33. Du, X., Zhao, G., Wang, W., Guo, M., Zhang, R., Yang, J.: NLIGA: A MATLAB framework for nonlinear isogeometric analysis. Comput. Aided Geom. Des. **80**, 101869 (2020)
34. Hill, R.: Theory of mechanical properties of fiber-strengthened materials: I. elastic behavior. J. Mech. Phys. Solids **12**, 199–212 (1964)
35. Chen, Q., Du, X., Wang, W., Chatzigeorgiou, G., Meraghni, F., Zhao, G.: Isogeometric homogenization of viscoelastic polymer composites via correspondence principle. Compos. Struct. **323**, 117475 (2023)
36. Piegl, L., Tiller, W.: Rational B-spline curves and surfaces. In: Piegl, L., Tiller, W. (eds.) The NURBS book, pp. 117–139. Springer, Berlin (1995)
37. Bensoussan, A., Lions, J.-L., Papanicolau, G.: Asymptotic analysis for periodic structures. Elsevier, Amsterdam (1978)
38. He, Z., Pindera, M.-J.: Finite volume-based asymptotic homogenization of periodic materials under in-plane loading. J. Appl. Mech. **87**, 121010 (2020)
39. Otero, J.A., Rodríguez-Ramos, R., Guinovart-Díaz, R., Cruz-González, O.L., Sabina, F.J., Berger, H., et al.: Asymptotic and numerical homogenization methods applied to fibrous viscoelastic composites using Prony's series. Acta Mech. **231**, 2761–2771 (2020)
40. Cavalcante, M.A.A., Khatam, H., Pindera, M.-J.: Homogenization of elastic–plastic periodic materials by FVDAM and FEM approaches—an assessment. Compos. B Eng. **42**, 1713–1730 (2011)
41. Chatzigeorgiou G, Charalambakis N, Chemisky Y, Meraghni F. 1 - Mathematical Concepts. In: Chatzigeorgiou G, Charalambakis N, Chemisky Y, Meraghni F, editors. Thermomechanical Behavior of Dissipative Composite Materials: Elsevier; 2018. p. 1–36.
42. Duan, H.L., Wang, J., Karihaloo, B.L., Huang, Z.P.: Nanoporous materials can be made stiffer than non-porous counterparts by surface modification. Acta Mater. **54**, 2983–2990 (2006)
43. Du, X., Zhao, G., Zhang, R., Wang, W., Yang, J.: Numerical implementation for isogeometric analysis of thin-walled structures based on a Bézier extraction framework: nligaStruct. Thin-Walled Struct. **180**, 109844 (2022)
44. Rodríguez-Ramos, R., de Medeiros, R., Guinovart-Díaz, R., Bravo-Castillero, J., Otero, J.A., Tita, V.: Different approaches for calculating the effective elastic properties in composite materials under imperfect contact adherence. Compos. Struct. **99**, 264–275 (2013)
45. Würkner, M., Berger, H., Gabbert, U.: Numerical investigations of effective properties of fiber reinforced composites with parallelogram arrangements and imperfect interface. Compos. Struct. **116**, 388–394 (2014)

Publisher's Note Springer Nature remains neutral with regard to jurisdictional claims in published maps and institutional affiliations.